



HAL
open science

Thermal conductivity, heat capacity and thermal expansion of ettringite and metaettringite: Effects of the relative humidity and temperature

Tulio Honorio

► **To cite this version:**

Tulio Honorio. Thermal conductivity, heat capacity and thermal expansion of ettringite and metaettringite: Effects of the relative humidity and temperature. *Cement and Concrete Research*, 2022, 159, pp.106865. 10.1016/j.cemconres.2022.106865 . hal-03693857

HAL Id: hal-03693857

<https://hal.science/hal-03693857>

Submitted on 22 Jul 2024

HAL is a multi-disciplinary open access archive for the deposit and dissemination of scientific research documents, whether they are published or not. The documents may come from teaching and research institutions in France or abroad, or from public or private research centers.

L'archive ouverte pluridisciplinaire **HAL**, est destinée au dépôt et à la diffusion de documents scientifiques de niveau recherche, publiés ou non, émanant des établissements d'enseignement et de recherche français ou étrangers, des laboratoires publics ou privés.



Distributed under a Creative Commons Attribution - NonCommercial 4.0 International License



Contents lists available at ScienceDirect

Cement and Concrete Research

journal homepage: www.elsevier.com/locate/cemconres



Thermal conductivity, heat capacity and thermal expansion of ettringite and metaettringite: Effects of the relative humidity and temperature

Tulio Honorio

Université Paris-Saclay, CentraleSupélec, ENS Paris-Saclay, CNRS, LMPS - Laboratoire de Mécanique Paris-Saclay, 91190, Gif-sur-Yvette, France

ARTICLE INFO

Keywords:

Thermal properties
Molecular dynamics
Green-Kubo formalism
Quantum corrections
Metaettringite

ABSTRACT

Thermal processes play a crucial role in the durability problems related to ettringite formation and the applications of ettringite for thermal energy storage. The complete characterization of the thermal response of ettringite requires the knowledge of how the thermoelastic properties of the materials evolve with the relative humidity and temperature. Here, molecular dynamics simulations are deployed to provide ettringite's thermoelastic properties, including the collapsing ettringite and metaettringite domains. The thermoelastic properties remain stable for RH ranging from 10 to 100 % at ambient temperature. The properties evolve linearly with the temperature in the range 278–328 K. Results from simulations show a good agreement with the experimental data available, building confidence in the use of molecular simulations to provide the property data in the conditions in which there is no experimental data available (as is the case of low RH conditions).

1. Introduction

Thermal processes in ettringite play a critical role in delayed ettringite formation, a significant durability problem involving ettringite [1]. Applications of ettringite-rich materials for thermal energy storage (TES) require a precise control of the thermal response of the material [2–5]. Thermal conductivity is the leading property controlling thermal transport; heat capacity, coefficient of thermal expansion, and elastic constants are fundamental to characterize thermoelastic behavior. Despite the importance of knowing precisely these properties to predict ettringite-rich materials behavior, to date, how the thermoelastic properties of ettringite and metaettringite evolve with the temperature and relative humidity remains unknown.

Gathering fundamental component data in cement systems has been highlighted as a task with the potential to revolutionize cement and concrete research [6]. Modeling strategies, especially atomistic simulations, play a leading role in this task. These simulations have been successfully deployed to understand the physical origins of various properties, including the thermal properties [7–9], of the different phases present in cement systems. In the case of ettringite, atomistic simulations provide estimations of the mechanical properties in agreement in experimental data [10–15]. Sorption and interfacial properties of ettringite were also successfully simulated using atomistic approaches [16,17]. At low RH (<1 %), ettringite dehydrates, forming a more disordered phase called metaettringite [18], whose structural details

have been only recently described, and that via atomistic simulations [17]. These results build confidence in the use of atomistic simulations to provide estimations of ettringite physical properties.

Atomistic simulations focusing on all the relevant thermal properties of ettringite have not yet been proposed in the literature. A first estimation of the thermal conductivity of ettringite has only been provided recently [19] and that solely for the saturated case under ambient temperature. Ettringite exhibits significant water content and volume changes under relative humidity (RH) and temperature variations [20,21]. The evolution of the thermal properties with the variation in the water content has been pointed out as a critical open question in TES applications of ettringite [2]. Such kind of information might help in the optimization of the domain of performance [18,21] of ettringite-rich products in TES. Further, the evolution of the thermoelastic properties of ettringite with the temperature is also valuable input for multiscale modeling.

In this work, molecular dynamics simulations are used to compute the thermoelastic properties of ettringite using classical molecular simulations. Thermal conductivity is calculated using standard Green-Kubo formalism and complex frequency-dependent conductivity. The heat capacity is calculated using classical and semi-classical approaches. The thermal expansion is computed using the fluctuation approach. The full stiffness tensor is calculated using finite differences. Configurations at equilibrium at ambient temperature and under various RH, as provided in ref. [17], are used as input. These configurations include

E-mail address: tulio.honorio-de-faria@ens-paris-saclay.fr.

<https://doi.org/10.1016/j.cemconres.2022.106865>

Received 5 June 2021; Received in revised form 30 May 2022; Accepted 30 May 2022

Available online 11 June 2022

0008-8846/© 2022 Elsevier Ltd. All rights reserved.

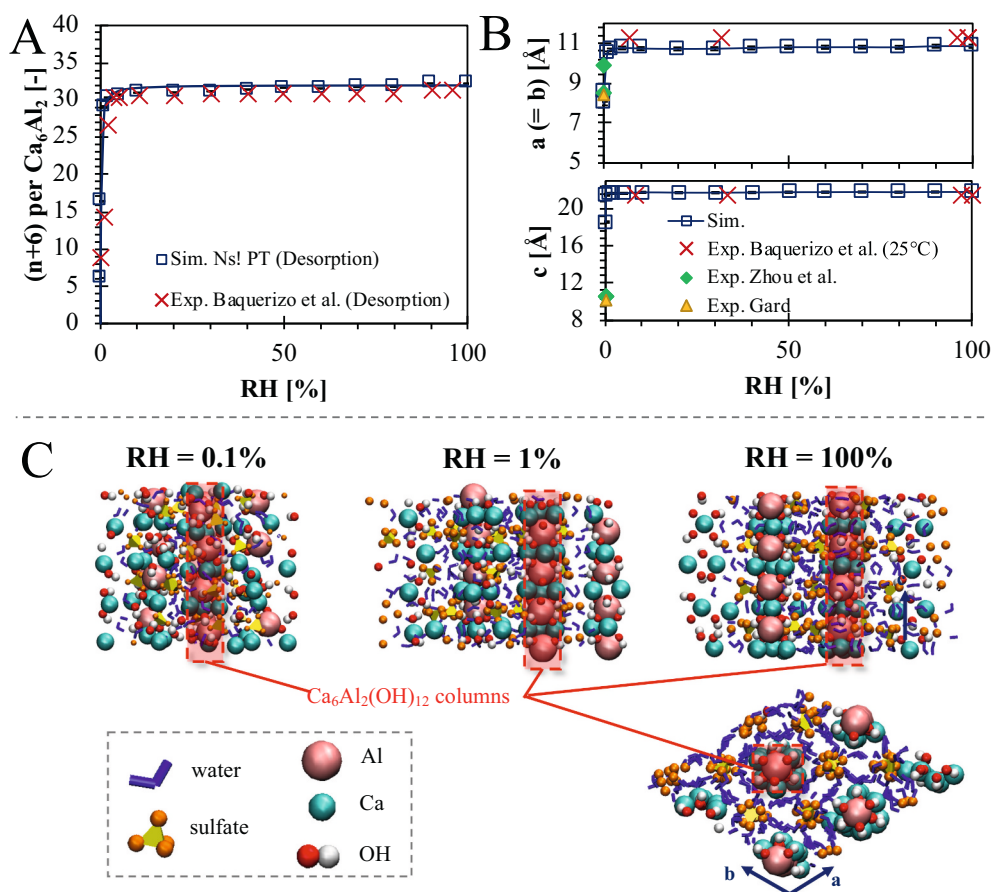


Fig. 1. (A) Desorption isotherm and (B) lattice parameters of ettringite: direct simulation in the osmotic ensemble ($N_s\mu\text{PT}$) [17] compared against the experimental results of Baquerizo et al. [21]. For the lattice parameters the experimental data of Zhou et al. [18] and Gard (as cited by [18]) are also shown. (C) Snapshots obtained from $N_s\mu\text{PT}$ simulations of ettringite-metaettringite structures along c -axis (top) and of ettringite at 100 %RH on ab plan (bottom). The red transparent boxes indicate $\text{Ca}_6\text{Al}_2(\text{OH})_{12}$ columns. (For interpretation of the references to color in this figure legend, the reader is referred to the web version of this article.)

systems in the metaettringite and collapsing ettringite domain. The interactions among atoms are modeled using the updated version [17] of empirical force field AFFF [14]. The updated version introduces harmonic covalent bonds and angles for sulfates. Finally, the temperature dependence of thermoelastic properties in the ettringite, collapsing ettringite, and metaettringite domains is quantified.

2. Molecular models and methods

2.1. Atomic structure and force field

The atomic structure of ettringite from ref. [22] is adopted. The structure is hexagonal with a P31c group. In the molecular formula of ettringite $\text{Ca}_6\text{Al}_2(\text{SO}_4)_3(\text{OH})_{12}\cdot n\text{H}_2\text{O}$ the molecular water content is variable with $n = 24-27$. This water content is associated with systems at equilibrium between 2 and 100 % RH at ambient temperature (and that according to a desorption process, since ettringite exhibits a pronounced hysteresis under sorption [17]). At lower RH, ettringite converts into metaettringite, which exhibits a lower water content ($n=5-7$ according to [18]). Significant changes in the structure are observed for $n < 24$ with a decrease in lattice parameters with dehydration with a subsequent collapse of the columnar structure of ettringite for $n < 12$ [18]. Hereafter, three domains are defined:

- *Ettringite domain* with water content $n = 24-27$ (corresponding RH: 5–100 % at ambient temperature)
- *Collapsing ettringite domain* with water content $n = 12-24$ (corresponding RH: 1–5 % at ambient temperature)
- *Metaettringite domain* with water content $n = 6-12$ (corresponding RH: 0–1 % at ambient temperature)

It must be noted that metaettringite is representative of the behavior in the adsorption branch up to RH of at least 60 % [17].

In a previous study [17], hybrid GCMC-MD simulations directly sampling the osmotic ensemble ($N_s\mu\text{PT}$) were deployed to obtain configurations at equilibrium according to various RH at 298 K. In an $N_s\mu\text{PT}$ simulation, the number of particles in the sorbent N_s , the chemical potential of water μ (directly related to the RH), the pressure P , and the temperature T are kept constant (while, the conjugate variables: the number of water molecules, the volume and the entropy are allowed to vary). The simulation outputs are in agreement with experimental data [21] regarding the water content and the lattice parameters, as shown in Fig. 1(A) and (B), respectively. The configurations for the various RH are used as input here. Fig. 1 (right) shows snapshots of the corresponding structures at equilibrium at various RH.

Atoms interactions are described using the empirical force field AFFF [14,17], which captures the structural features, elastic response, and sorption behavior of ettringite [14,17]. AFFF uses flexible SPC/E to model water and OH groups in the columns; the associated bond and angles are based on ClayFF parameters [23]. In the last version of AFFF, bond and angles interactions [17] are introduced for sulfates to capture the structural changes under sorption-induced deformations better. As shown in Section 3.1.3, this feature improves the estimation of elastic constants. However, rigid water model captures better the experimental thermal conductivity (see Appendix A) and heat capacity of water [24]. Therefore, rigid models are adopted for these properties.

Simulation is run with LAMMPS [25]. A cutoff of 10 Å is used for non-bond pair interactions. Tails corrections are used for Lennard-Jones potential; Ewald summation is deployed to cope with long-range electrostatics (with a relative error in forces of 10^{-5}). Time integration is performed using a 0.1 fs timestep.

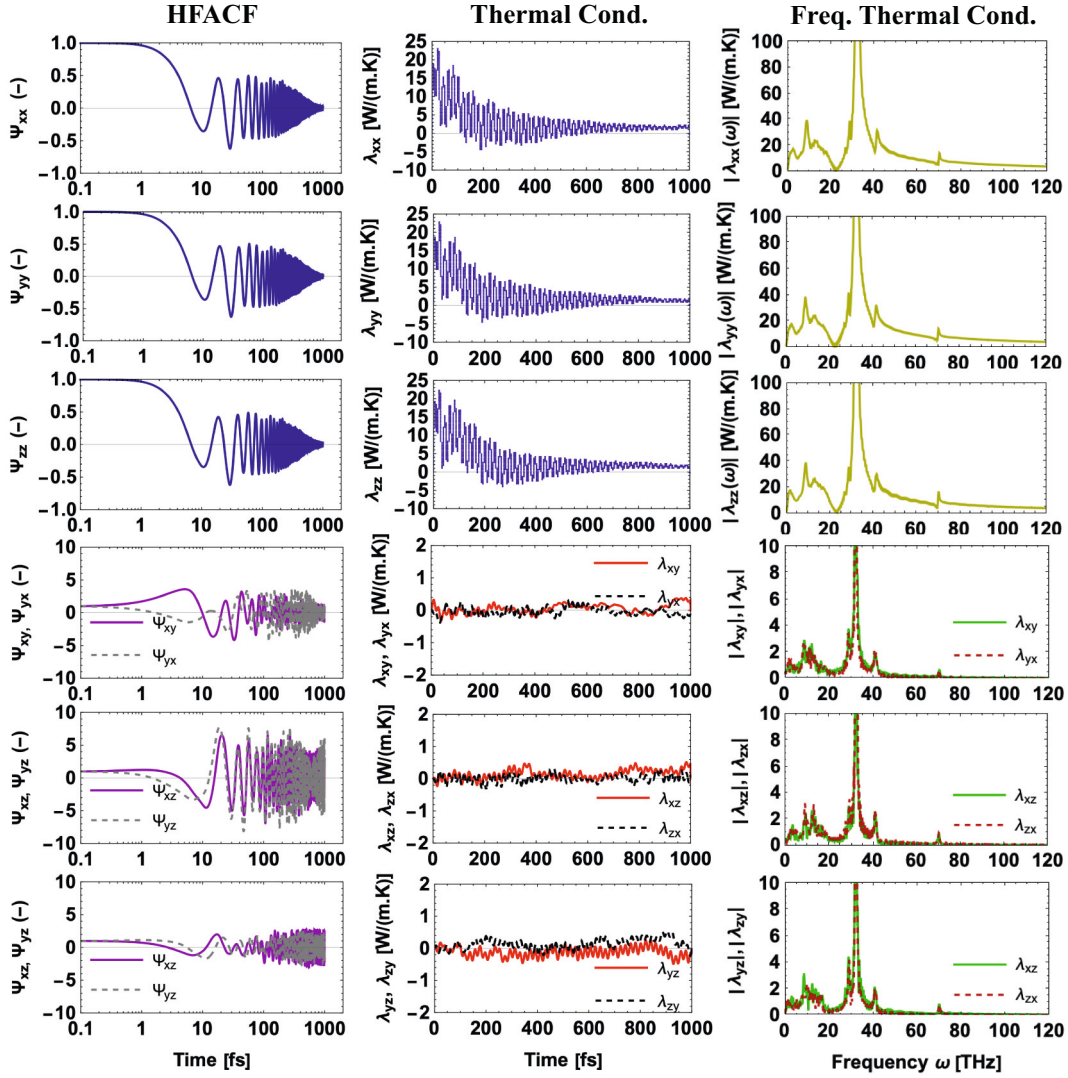


Fig. 2. At left, components of the heat flux auto-correlation function (HFACF) of ettringite at RH = 100 % and at ambient temperature (298 K) as a function of the simulation time. At center, components of the thermal conductivity obtained from direct integration of the HFACFs according to the standard Green-Kubo formalism (Eq. (1)) as a function of the simulation time. At right, components of the complex frequency-dependent thermal conductivity (Eq. (3)) as a function of the simulation time. All results are reported in a Cartesian frame ((x, y, z), where $x \equiv a$ and $z \equiv c$).

2.2. Thermoelastic properties from molecular simulations

2.2.1. Thermal conductivity

The thermal conductivity tensor can be computed from molecular simulations using equilibrium and non-equilibrium methods. Non-equilibrium methods include direct thermostating method [26], and reverse perturbation method [27]. The main equilibrium method is the Green-Kubo formalism, adopted in this work and detailed in the following.

Using Green-Kubo formalism, the thermal conductivity is the time integral of the ensemble average (denoted by $\langle \cdot \rangle$ operator) of the heat flux J_i ($i = x, y, z$) auto-correlation (e.g. [28]):

$$\lambda_{ij} = \frac{V}{kT^2} \int_0^\infty \langle J_i(0) \otimes J_j(t) \rangle dt \quad (1)$$

where V is the volume, T is the temperature, k is the Boltzmann constant and \otimes stands for the tensor product. The terms $\Phi_{ij} = \langle J_i(0) \otimes J_j(t) \rangle$ are the components of the heat flux auto-correlation function (HFACF). The heat flux vector is computed from the virial stress, kinetics and potential energy per atom:

$$\mathbf{J}_p = \frac{1}{V} \left[\sum_p E_p \mathbf{v}_p - \sum_p \mathbf{S}_p \mathbf{v}_p \right] \quad (2)$$

where E_p is the sum of the kinetics and potential energy, \mathbf{v} is the velocity vector, and \mathbf{S}_p is the stress tensor for atom p .

The conductivity λ_{ij} computed from Eq. (1) may not converge as $t \rightarrow \infty$ in the integration. A solution to overcome this problem is to compute the thermal conductivity tensor using the frequency-dependent response of the complex conductivity [29]:

$$\lambda_{ij}(\omega) = \frac{V}{kT^2} \int_0^\infty \langle J_i(0) \otimes J_j(t) \rangle \exp[i\omega t] dt \quad (3)$$

The static thermal conductivity λ_{ij}^0 can be obtained from fitting, in the low frequency range, the modulus $|\lambda_{ij}(\omega)|$ of the complex conductivity with the expression $|\lambda_{ij}(\omega)| = \lambda_{ij}^0 + A\omega^\xi$, where λ_{ij}^0 , A and ξ are free parameters in the fitting procedure [7].

Regarding the simulations, prior to the computation of heat fluxes, the systems are equilibrated during 0.5 ns in an NVT run (Nosé-Hoover thermostat with a damping parameter of 100 timesteps is adopted). Then, to avoid the fictitious forces due to the thermostat affecting the

computation of the thermal conductivity, the heat fluxes are computed in an NVE run (it was verified that the target temperature is stable during this run). An extensive convergence study of the correlation lengths and timesteps was performed. The HFACF shows a high oscillatory pattern, which is well captured by the 0.1 fs adopted here. The diagonal components of the HFACF decay to zero within the 1 ps window; the out-of-diagonal components oscillated around zero. These aspects are depicted in Fig. 2 for the case of ettringite at RH = 100 % and T = 298 K. The direct integration of these HFACFs according to the standard Green-Kubo formalism (Eq. (1)) shows convergence for a correlation length of 1 ps. For production, 20 independent trajectories are considered for each RH and temperature. Each trajectory comprises a 20 ps run in which the HFACF is accumulated during this running with a sample interval of 1 timestep. Standard deviations for the components of the thermal conductivity tensor are computed from converged results in the 20 independent trajectories.

The complex frequency-dependent thermal conductivity (Eq. (3)) is also depicted in Fig. 2. In the results section, the outcomes obtained using this strategy are compared with the results from standard Green-Kubo formalism.

In the strategy presented above, the required symmetry of λ_{ij} is not enforced. Verification of such symmetry is also illustrated by the results shown in Fig. 2. The out-of-diagonal HFACF components are similar, and the symmetry $\lambda_{ij} = \lambda_{ji}$ is approximately observed for both cases (of direct integration and complex frequency-dependent thermal conductivity).

2.2.2. Coefficient of thermal expansion

The tensor of thermal expansion can be computed from the definition (e.g. [30,31]):

$$\alpha_{ij} = \left[\frac{\partial \varepsilon_{ij}}{\partial T} \right]_{\sigma_{ij}} \quad (4)$$

or using a the fluctuation formula [30–32]:

$$\alpha_{ij} = \frac{\langle H \varepsilon_{ij} \rangle_{N\sigma T} - \langle H \rangle_{N\sigma T} \langle \varepsilon_{ij} \rangle_{N\sigma T}}{kT^2} \quad (5)$$

where the thermal expansion tensor can be obtained from the cross fluctuations of the enthalpy H and the second-order Lagrangian deformation tensor $\varepsilon_{ij} = \frac{1}{2} [\mathbf{h}_0^{-T} \mathbf{h}^T \mathbf{h} \mathbf{h}_0^{-1} - \mathbf{I}]$, obtained from the crystal cell parameters (\mathbf{h} matrix is a matrix formed by arranging the lattice vectors as $\{\mathbf{a}, \mathbf{b}, \mathbf{c}\}$, the subscript 0 refers to the reference zero stress state). \mathbf{I} is the unit 3×3 matrix, and the superscript $[\cdot]^T$ is the transpose operator.

The simulations are performed with the fluctuation approach in $N\sigma T$ ensemble with Nosé-Hoover thermostat and barostat (the barostat is applied independently according to each direction of the stress tensor) during 0.5 ns production run after proper equilibration. The enthalpy and enthalpy/deformation cross-terms are averaged during these 0.5 ns. Five independent trajectories are considered, and the standard deviation from these trajectories.

2.2.3. Heat capacity

In a full classical approach, the heat capacity can be computed in a molecular simulation using the definitions

$$C_V = \left[\frac{\partial E}{\partial T} \right]_V; C_P = \left[\frac{\partial H}{\partial T} \right]_P \quad (6)$$

and a finite difference method, or by means of fluctuation-dissipation formula [33]:

$$C_V = \frac{\langle E^2 \rangle_{NVT} - \langle E \rangle_{NVT}^2}{kT^2} \quad (7)$$

$$C_P = \frac{\langle H^2 \rangle_{NPT} - \langle H \rangle_{NPT}^2}{kT^2} \quad (8)$$

where V and P are the volume and pressure, and E is the internal energy.

For comparison with experimental data, it can be helpful to report the heat capacities in terms of specific heat capacities c_V, c_P (in a unit of energy per mass-Kelvin). The specific heat capacities can be computed from the total heat capacity C_V, C_P using $c_V = C_V/(m_{total})$ and $c_P = C_P/(m_{total})$, with m_{total} being the mass.

Various authors show that the incorporation of quantum corrections are often required to properly reproduce the experimental heat capacity of crystalline materials [7,34–36]. Due to the high phonon frequency in crystals (i.e., when $\hbar\omega \sim kT$ in ambient conditions), quantum effects become non-negligible, leading to a heat capacity lower than the classical estimate may yield. A semi-classical approach can be defined in which quantum effects are incorporated but the vibrational density of states is obtained using classical methods [37,38]. In this approach, the heat capacity at constant volume is

$$C_V = \frac{dE_{vib}}{dT} = 3Nk \int_0^\infty \left(\frac{\hbar\omega n(\omega, T)}{kT} \right)^2 \exp\left[\frac{\hbar\omega}{kT}\right] g(\omega) d\omega \quad (9)$$

where $3Nk$ corresponds to the Dulong-Petit law, ω is the angular frequency, \hbar is the reduced Planck constant, $n(\omega, T)$ is Bose-Einstein distribution $n(\omega, T) = \frac{1}{\exp(\frac{\hbar\omega}{kT}) - 1}$, and $g(\omega)$ is the vibrational density of the states (VDOS) [37,38]:

$$g(\omega) = \frac{1}{\pi} \int_{-\infty}^\infty \sum_j \frac{\langle m_j \mathbf{v}_j(t) \cdot \mathbf{v}_j(0) \rangle}{\langle m_j \mathbf{v}_j^2(0) \rangle} \exp[i\omega t] dt \quad (10)$$

The VDOS is obtained from the mass-weighted velocity auto-correlation function $\langle m_j \mathbf{v}_j(t) \cdot \mathbf{v}_j(0) \rangle$, with m_j being the mass of particle j ; and $\mathbf{v}_j(t)$ being the velocity vector of particle j at time t .

A hybrid approach combining the semi-classical method for the dry mineral and a classical approach for the water has been shown to best capture the heat capacity of hydrated minerals such as swelling clays [24]. A way of computing the heat capacity via this hybrid approach is first to compute the classical approach for the entire system (C_V^{class}) and then subtract the contribution of the dry mineral (the classical approach applied to the dry mineral yields Dulong-Petit law ($C_{V-min}^{class} = 3N_s k$ [24])). The contribution of water in the classical approach is therefore $C_{V-w}^{class} = C_V^{class} - 3N_s k$. The total heat capacity is then obtained as the sum of the inter-layer and dry mineral ($C_{V-min}^{semi-class}$) contributions:

$$C_V = C_{V-w}^{class} + C_{V-min}^{semi-class} = C_V^{class} - 3N_s k + C_{V-min}^{semi-class} \quad (11)$$

where $C_{V-min}^{semi-class}$ is computed from the semi-classical approach detailed above applied only to the dry mineral.

In the hybrid approach, the specific heat capacities are given by [24]:

$$c_V = f_w c_{V-w}^{class} + (1 - f_w) c_{V-min}^{semi-class} = c_V^{class} + (1 - f_w) \left(c_{V-min}^{semi-class} - \frac{3N_s k}{m_s} \right) \quad (12)$$

with $f_w = m_w/m_{total}$ and $(1 - f_w = m_s/m_{total})$ being the mass fractions of water and dry mineral, respectively.

The difference between c_P and c_V is given using Mayer's relation (e.g. [39]):

$$c_P - c_V = \frac{T}{\rho} C_{ijkl} \alpha_{ij} \alpha_{kl}, \quad (13)$$

where ρ is the density.

Full classical simulations are performed with the fluctuation approach in the NVT ensemble with a 0.1 fs timestep, 0.1 ns are used to equilibrate the system followed by a 0.5 ns production run. The internal energy and its square are averaged during these 0.5 ns. Semi-classical simulations are performed in the NVE ensemble (again, to avoid the fictitious forces from the thermostats) in 10 ps runs following proper equilibration (under NVT ensemble). Appendix B shows the velocity and

Table 1

Thermal properties of ettringite, collapsing ettringite, and metaettringite at $T = 298$ K. Tensorial quantities are symmetrized (i.e., $\lambda_{ij} = \frac{1}{2}(\lambda_{ij} + \lambda_{ji})$ and $\alpha_{ij} = \frac{1}{2}(\alpha_{ij} + \alpha_{ji})$). The hybrid approach combining classical and semi-classical methods is deployed for the heat capacity. Molecular water content n given according to the structural formula $\text{Ca}_6\text{Al}_2(\text{SO}_4)_3(\text{OH})_{12}\cdot n\text{H}_2\text{O}$ (with the total water content accounting also for OH groups in the columns being $(n + 6)$).

RH	Ettringite	Collap-ettr.	Meta-ettr.
n	5–100 %	1 %	0.1 %
	24–27	23	10
λ_{xx} [W/(m·K)]	3.09 ± 0.90	3.34 ± 0.73	1.43 ± 0.52
λ_{yy} [W/(m·K)]	2.83 ± 0.85	4.95 ± 0.72	1.74 ± 0.56
λ_{zz} [W/(m·K)]	2.41 ± 0.88	5.06 ± 0.74	3.00 ± 0.82
λ_{xy} [W/(m·K)]	0.03 ± 1.17	-5.66 ± 2.10	-0.38 ± 1.53
λ_{xz} [W/(m·K)]	0.32 ± 1.14	-1.54 ± 2.75	-0.19 ± 1.71
λ_{yz} [W/(m·K)]	0.33 ± 1.21	3.27 ± 4.11	0.89 ± 1.68
λ_{11} [W/(m·K)]	4.87	8.05	3.12
λ_{22} [W/(m·K)]	2.33	4.12	1.61
λ_{33} [W/(m·K)]	1.13	1.18	1.45
λ_v [W/(m·K)]	2.78 ± 0.51	4.45 ± 0.73	2.06 ± 0.65
α_{xx} [$10^{-5}/\text{K}$]	4.40 ± 0.63	4.10 ± 1.40	4.61 ± 1.16
α_{yy} [$10^{-5}/\text{K}$]	4.41 ± 0.63	4.13 ± 1.39	4.62 ± 1.18
α_{zz} [$10^{-5}/\text{K}$]	6.67 ± 0.52	6.21 ± 3.06	3.47 ± 1.38
α_{xy} [$10^{-5}/\text{K}$]	-0.30 ± 1.56	-1.87 ± 1.97	0.69 ± 1.97
α_{xz} [$10^{-5}/\text{K}$]	0.46 ± 1.11	-0.75 ± 1.44	0.84 ± 1.44
α_{yz} [$10^{-5}/\text{K}$]	0.48 ± 1.00	-1.23 ± 1.74	0.41 ± 1.74
α_{11} [$10^{-5}/\text{K}$]	7.61	6.80	5.67
α_{22} [$10^{-5}/\text{K}$]	5.03	5.85	4.01
α_{33} [$10^{-5}/\text{K}$]	2.83	1.79	3.02
α_v [$10^{-5}/\text{K}$]	15.45 ± 1.03	14.4 ± 3.87	13.91 ± 1.35
c_v [J/(kg·K)]	1746 ± 48	1805 ± 39	1366 ± 21
c_p [J/(kg·K)]	1845 ± 75	1879 ± 74	1422 ± 75

mass-weighted velocity autocorrelation functions and the vibrational density of states for ettringite and metaettringite. Five independent trajectories are considered in both full and semi-classical cases, and the

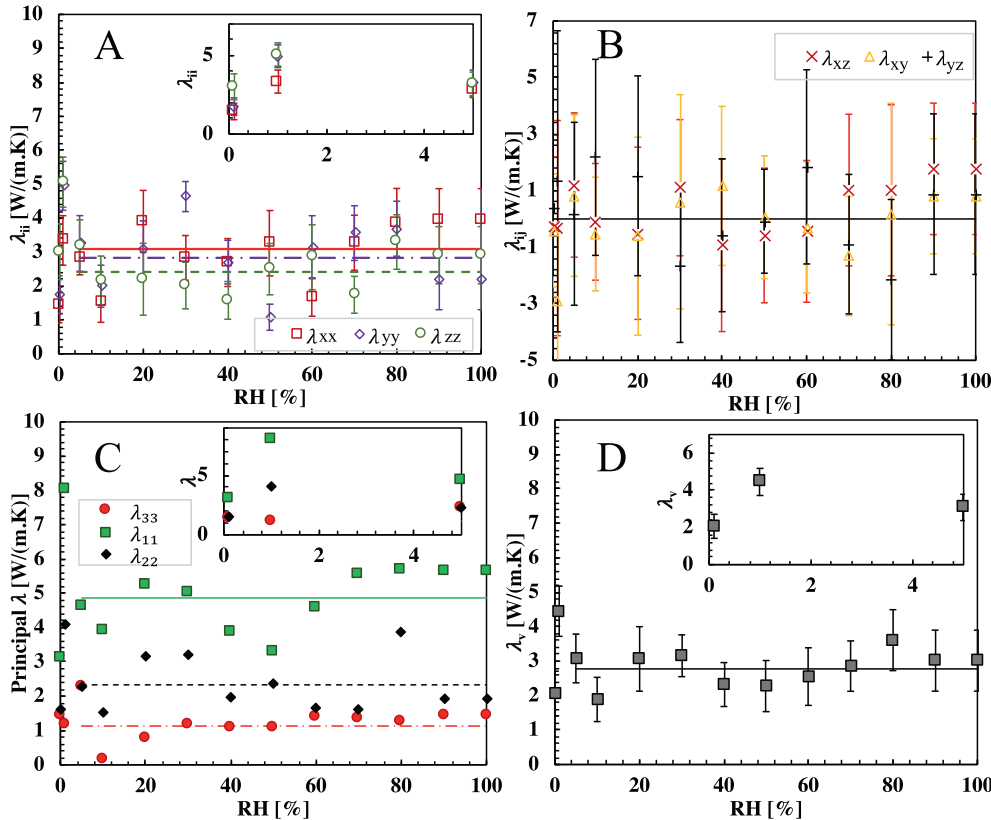


Fig. 3. Components of the tensor of thermal conductivity of ettringite (and metaettringite) at ambient temperature (298 K) in a Cartesian frame $((x, y, z))$, where $x \equiv a$ and $z \equiv c$: (A) diagonal λ_{ii} , and (B) out-of-diagonal $\lambda_{ij}(i \neq j)$ components. In (A) the lines show the average conductivity values in the ettringite domain (RH > 1%). (C) Principal components of the tensor of thermal conductivity of ettringite and metaettringite. (D) Volumetric thermal conductivity ($\lambda_c = \text{Tr}(\lambda) / 3$) of ettringite and metaettringite as a function of RH. Five MD trajectories are considered for computing the standard deviations. The insets zoom in the low RH domain.

standard deviation is calculated from the c_v obtained for each trajectory.

2.2.4. Elastic constants

Despite the focus of this work being on thermal properties, the elastic constants are required to compute $c_p - c_v$ (Eq. (13)).

The elastic constants are computed using a finite difference approach using the definition [33]:

$$C_{ijkl} = \left[\frac{\partial \sigma_{ij}}{\partial \epsilon_{kl}} \right]_{T, \epsilon_{kl}} \quad (14)$$

in which σ is the second-rank stress tensor.

The finite difference approach (here, under finite temperature) consists of slightly deforming (so that the system remains within the elastic domain) the simulation box in each one of the six axial and tangential directions followed by an NVT run in which the ensemble-averaged pressure tensor is computed. To avoid the effects of any tension-compression asymmetry under loading, the average of both negative and positive deformations is considered in the computations.

3. Results and discussion

3.1. Thermoelastic properties of ettringite and metaettringite at ambient temperature: effects of the RH

Table 1 gathers the thermal properties of ettringite and metaettringite at ambient temperature. For the tensorial quantities, the results are shown in both Cartesian and principal frames. Details on the computation and a comparison with available data from the literature are presented in the following.

3.1.1. Thermal conductivity

The components of the tensor of thermal conductivity of ettringite and metaettringite (in a Cartesian frame $((x, y, z))$) obtained from MD

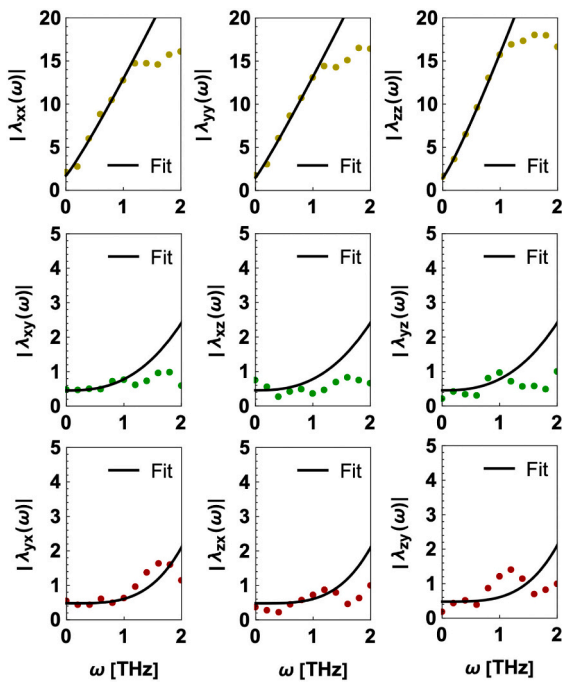


Fig. 4. Components of the complex frequency-dependent thermal conductivity at low frequency and fittings for the case of ettringite at ambient temperature (298 K) in a Cartesian frame ((x, y, x)).

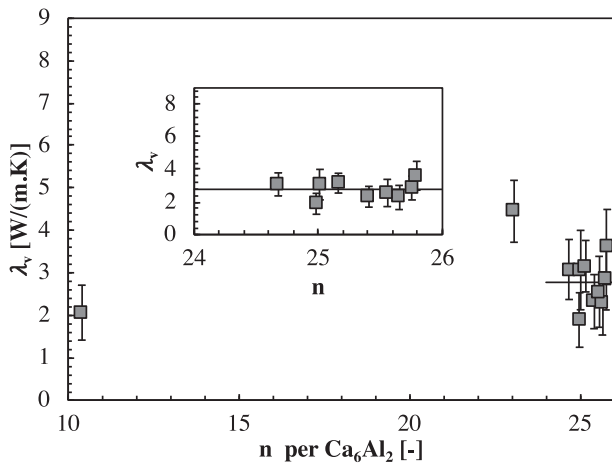


Fig. 5. Volumetric thermal conductivity ($\text{Tr}(\lambda) / 3$) of ettringite (and metaettringite) at ambient temperature (298 K) as a function of the water content. The line shows the average conductivity values in the ettringite domain (RH > 10 %). The inset zooms in the ettringite domain.

simulations are shown in Fig. 3(A) and (B). In the ettringite domain, on average, the diagonal components follow $\lambda_{xx} > \lambda_{yy} > \lambda_{zz}$ ($3.09 \pm 0.90 > 2.83 \pm 0.85 > 2.41 \pm 0.88$ W/(m·K)), as indicated by the horizontal lines in Fig. 3(A). The out-of-diagonal components $\lambda_{ij} (i \neq j)$ (Fig. 3(B)) are close to zero (considering the standard deviation of the simulations). The results obtained by direct integration of HFACF agree with the one obtained using the complex frequency-dependent conductivity. Fig. 4 shows the complex frequency-dependent thermal conductivity at low frequency and corresponding fittings for the case of ettringite at ambient temperature.

The principal components (eigenvalues) of the thermal conductivity tensor are shown in Fig. 3(C). The average values of the principal components in the ettringite domain are $\lambda_{11} = 4.87$ W/(m·K), $\lambda_{22} = 2.33$ W/(m·K), $\lambda_{33} = 1.13$ W/(m·K), which shows a non-negligible anisotropy

Table 2

Thermal conductivity of hydrates and clinker minerals.

Phase	λ_v [W/(m·K)]	Ref.
Ettringite	2.76 ± 0.51	This work
Collap. ettringite	4.45 ± 0.73	This work
Metaettringite	2.06 ± 0.65	This work
C-S-H (Ca/Si = 1.0)	0.98 ± 0.2	[7]
C-S-H (Ca/Si = 1.75)	0.98 ± 0.2	[7]
Tobermorite 9 Å	1.470	[9]
Tobermorite 11 Å	3.577	[9]
Tobermorite 14 Å	4.510	[9]
Jennite	1.007	[9]
Jennite	1.136–1.164	[8]
Portlandite	1.32 ± 0.2	[7]
C ₃ S	3.35 ± 0.3	[7]
β -C ₂ S	3.45 ± 0.4	[7]

in the thermal conductivity.

The volumetric thermal conductivity $\lambda_v = \text{Tr}(\lambda_{ij}) / 3 = \sum \lambda_{ii} / 3$ (being an invariant, the trace $\text{Tr}(\cdot)$ can be computed using the thermal conductivity tensor in any frame) is shown in Fig. 3(D) as a function of the RH and in Fig. 5 as a function of the molecular water content. The variability observed in λ_v when plotted as a function of the RH in the ettringite domain is on the order of the standard deviation of the simulation results, with the values fluctuating around an average value (full line in Fig. 3(D), the average was taken over the range 5–100 % RH). In the ettringite domain, λ_v is 2.76 ± 0.51 W/(m·K). This value can be compared with the conductivity of ettringite recently reported in the literature of 2.19 ± 0.4 [19]. The values obtained at low RH are: for collapsing ettringite $\lambda_v = 4.45 \pm 0.73$ W/(m·K) (a surprising high value considering the typical conductivity of hydrated minerals and that is not yet supported by experimental evidence), and for metaettringite $\lambda_v = 2.06 \pm 0.65$ W/(m·K). Note that the value of thermal conductivity computed in the ettringite domain takes into consideration all the conductivities in the 10–100 %RH range (i.e. 10 values). The resulting thermal conductivity is, therefore, more precise than a single value. In contrast, only one point is considered in the conductivity of the metaettringite and collapsing ettringite; these values are therefore more prone to variability/uncertainty. In particular, the theoretical thermal conductivity obtained for collapsing ettringite being almost twice the values of ettringite and metaettringite raise questions about the precision and fidelity of the obtained value. The values for ettringite are on the range of the conductivity of minerals such as dolomite 3.1–5.1 W/(m·K) [40], other hydrates and clinker minerals (see Table 2).

3.1.2. Thermal expansion

Fig. 6(A) and (B) shows the components of the tensor of thermal expansion of ettringite (and metaettringite) at ambient temperature in the Cartesian frame. Due to the hexagonal symmetry $\alpha_{xx} \approx \alpha_{yy} \approx \alpha_a$ as expected. These values obtained are to be compared with the experimental results of Hall [41]: $\alpha_a = 4.2 \times 10^{-5}/\text{K}$ and $\alpha_c = 2.2 \times 10^{-5}/\text{K}$. The out-of-diagonal $\alpha_{ij} (i \neq j)$ components are close to zero with a larger deviation observed for α_{xy} which suggest a certain degree of coupling of thermal expansion in the plane perpendicular to the columns (so that tensor α would assume a form similar to that of the tensor of crystal shrinkage of ettringite in ref. [17] with all out-of-diagonal terms being negligible except α_{xy}). Fig. 6(C) shows the tensor of thermal expansion in its principal basis. The first principal value corresponds closely to α_c . The volumetric coefficient of thermal expansion ($\alpha_v = \text{Tr}(\alpha)$) is shown in Fig. 6(D) as a function of the RH and in Fig. 7 as a function of the water content. As for the other thermoelastic properties, the coefficient of thermal expansion remains stable for RH from 10 to 100 % (i.e., in the ettringite domain) with a slight decrease in the collapsing ettringite and metaettringite domains.

3.1.3. Elastic constants

The stiffness tensor of a hexagonal crystal has five independent non-

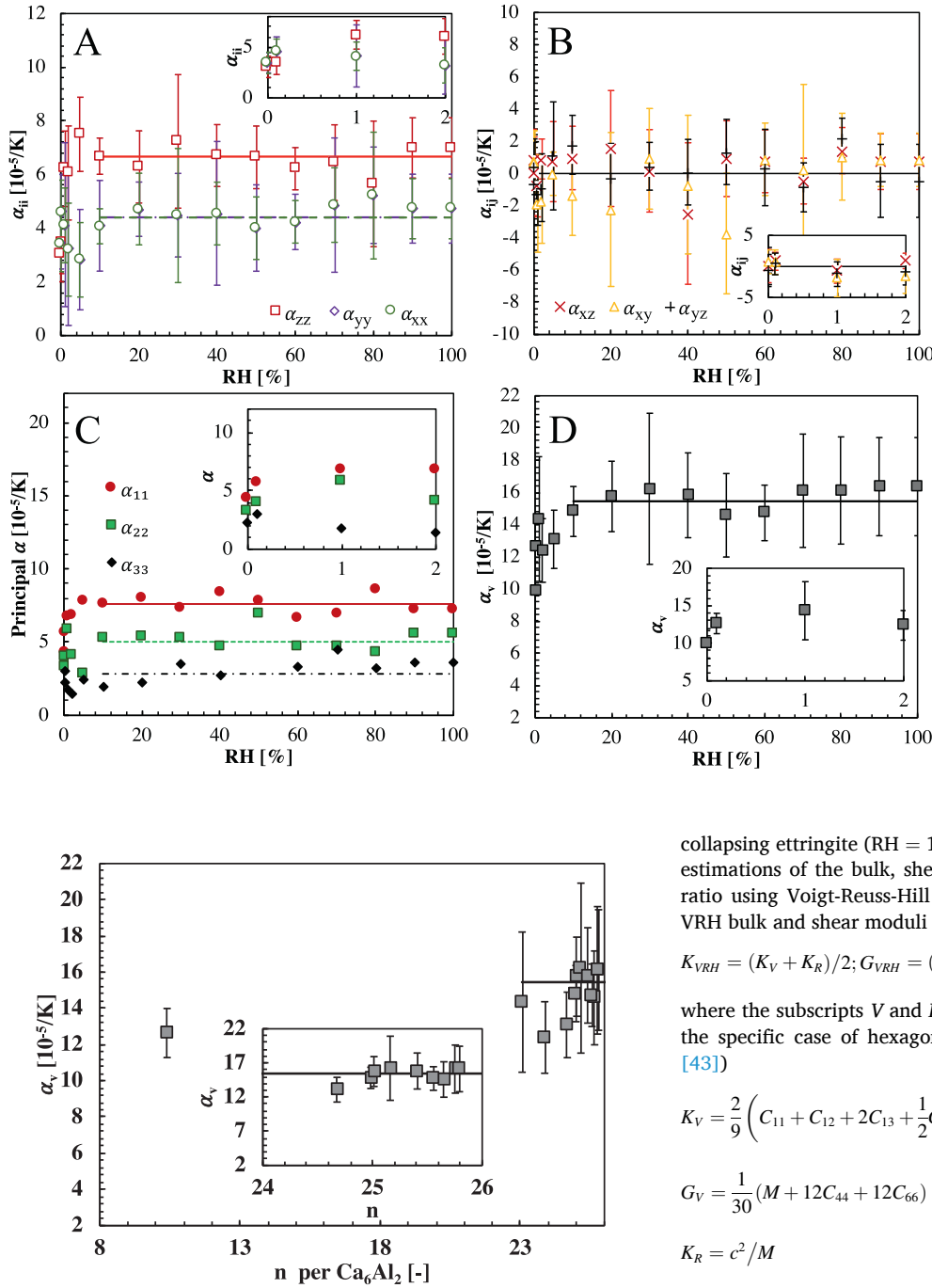


Fig. 7. Volumetric coefficient of thermal expansion ($\alpha_v = Tr(\alpha)$) of ettringite (and metaettringite) at ambient temperature (298 K) as a function of the water content. The line shows the average α_v in the ettringite domain (RH > 10 %). The inset zooms in the ettringite domain.

zero components (in Voigt notation): $C_{11}(=C_{22})$, C_{12} , $C_{13}(=C_{23})$, C_{33} and $C_{44}(=C_{55})$, with $C_{66} = (C_{11}-C_{12})/2$. Fig. 8 shows how these independent components evolve with the relative humidity and water content. Additionally, the evolution of C_{22} , C_{23} , C_{55} , C_{16} (expected to be zero), and C_{66} are to confirm that the crystal remains hexagonal under low RH conditions. Overall the elastic constants remain stable in the ettringite domain and slightly decrease in the collapsing ettringite and metaettringite domain. However, this decrease is in the order of the variability on the ettringite domain.

Table 3 gathers the elastic constants considering the average in the ettringite domain (RH = 10–100 %) and the structures associated with

Fig. 6. Components of the tensor of thermal expansion of ettringite (and metaettringite) at ambient temperature (298 K) in a Cartesian frame ((x,y,z), where $x \equiv a$ and $z \equiv c$): (A) diagonal α_{ii} , and (B) out-of-diagonal $\alpha_{ij}(i \neq j)$ components. In (A) the lines show the average thermal expansion values in the ettringite domain (RH > 5 %). (C) Principal components of the tensor of thermal expansion of ettringite and metaettringite. (D) Volumetric thermal expansion ($\alpha_v = Tr(\alpha)$) of ettringite and metaettringite as a function of RH. Five MD trajectories are considered to compute the standard deviations. The insets zoom in the low RH domain.

collapsing ettringite (RH = 1 %) and metaettringite (RH = 0.1 %). The estimations of the bulk, shear, and Young moduli, as well as Poisson ratio using Voigt-Reuss-Hill (VRH) approximation [42] are provided. VRH bulk and shear moduli read:

$$K_{VRH} = (K_V + K_R)/2; G_{VRH} = (G_V + G_R)/2; \quad (15)$$

where the subscripts V and R denote the Voigt and Reuss estimates. In the specific case of hexagonal symmetry, these estimates read (e.g., [43])

$$K_V = \frac{2}{9} \left(C_{11} + C_{12} + 2C_{13} + \frac{1}{2}C_{33} \right) \quad (16)$$

$$G_V = \frac{1}{30} (M + 12C_{44} + 12C_{66}) \quad (17)$$

$$K_R = c^2/M \quad (18)$$

$$G_R = \frac{5}{2} \frac{c^2 C_{44} C_{66}}{c^2 (C_{44} + C_{66}) + 3K_V C_{44} C_{66}} \quad (19)$$

with $M = C_{11} + C_{12} + 2C_{33} - 4C_{13}$ and $c^2 = (C_{11} + C_{12})C_{33} - 2C_{12}^2$. The VRH Young E_{VRH} modulus and the Poisson ratio ν_{VRH} can be computed from the VRH estimates: $E_{VRH} = 9K_{VRH}G_{VRH}/(3K_{VRH} + G_{VRH})$ and $\nu_{VRH} = (3K_{VRH} - 2G_{VRH})/(6K_{VRH} + 2G_{VRH})$.

The elastic tensors obtained from simulation are compared with the experimental data from Speziale et al. [44] for ettringite. To provide a single scalar indicator of how the results present here are close to the experimental data, the Riemannian metric (e.g. [45]):

$$d_R(M_1, M_2) \equiv \left\| \ln \left(M_2^{1/2} M_1^{-1} M_2^{1/2} \right) \right\|_R = \sqrt{\sum_{i=1}^n \ln^2 \lambda_i} \quad (20)$$

where M_1 and M_2 are two symmetric positive-definite matrices, λ_i are the

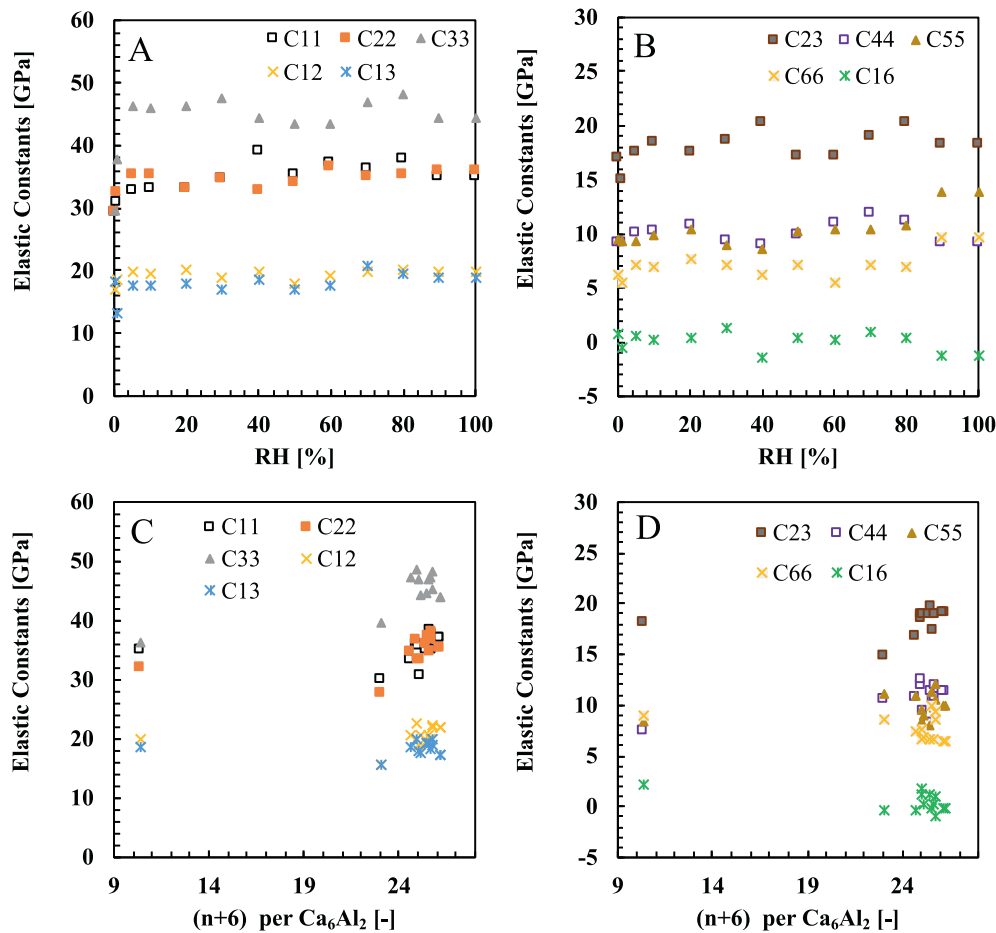


Fig. 8. Components of the rigidity tensor of ettringite (and metaettringite) at ambient temperature (298 K) as a function of the (A)–(B) RH and (C)–(D) water content.

Table 3

Components of stiffness tensor C_{ij} (Voigt notation); bulk K and shear G moduli according to Voigt (subscript V), Reuss (subscript R) and Voigt-Reuss-Hill (subscript VRH) approximation; Poisson ratio ν and Young modulus E ; universal anisotropy index A^u , and Riemannian d_R/d_0 metrics computed with respect to the experimental results provided by Speziale et al. [44] C_{ij}^{exp} , with $d_0 = \left\| C_{ij}^{\text{exp}} \right\|_E = \sqrt{\text{Tr} \left[\left(C_{ij}^{\text{exp}} \right)^T \left(C_{ij}^{\text{exp}} \right) \right]}$.

	Metaett. (RH = 0.1 %)	Collap. ettr. (RH = 1 %)	Ettringite AFFF ^a	Ettringite AFFF ^b	Ettringite exp. ^c
C_{11} [GPa]	34.7 ± 7.1	29.8 ± 2.5	35.6 ± 3.9	36.6	35.1 ± 0.1
C_{33} [GPa]	36.0 ± 5.4	39.3 ± 2.8	45.8 ± 3.1	47.5	55.0 ± 1
C_{12} [GPa]	19.8 ± 2.8	15.4 ± 1.7	20.9 ± 2.2	19	21.9 ± 0.1
C_{13} [GPa]	18.5 ± 3.5	15.6 ± 3.0	18.5 ± 2.1	15.9	20.0 ± 0.5
C_{44} [GPa]	7.3 ± 1.1	10.4 ± 2.1	10.8 ± 2.3	9.3	11.0 ± 0.2
C_{66} [GPa]	8.9 ± 2.7	8.6 ± 0.7	7.4 ± 2.0	10.7	6.6 ± 0.1
K_V [GPa]	24.3	21.3	25.8	24.7	27.7 ± 0.9
G_V [GPa]	8.3	9.6	9.8	10.9	9.9 ± 0.1
K_R [GPa]	22.4	21.3	23.1	22.1	26.9 ± 0.6
G_R [GPa]	8.1	9.5	9.2	10.4	9.0 ± 0.1
K_{VRH} [GPa]	23.3	21.3	24.5	23.4	27.3 ± 0.9
G_{VRH} [GPa]	8.2	9.6	9.5	10.7	9.5 ± 0.8
E_{VRH} [GPa]	21.9	25.0	25.2	27.8	25.0 ± 2
ν_{VRH} [-]	0.34	0.30	0.33	0.30	0.34 ± 0.01
A^u [-]	0.21	0.05	0.44	0.34	0.55
d_R/d_0	0.0095	0.0057	0.0028	0.007	0

^a This work with AFFF with covalent bonds and angles defined for sulfates as in ref. [17].

^b AFFF with no covalent bonds and angles defined for sulfates as in ref. [14].

^c Experiments from ref. [44].

eigenvalues of the matrix $M_1^{-1}M_2$, is deployed. This metric is invariant under inversion preserving material symmetry [45] and has been used in previous works to compare elastic tensors obtained from molecular simulations and experiments [14,46]. Riemannian metric is zero for two

identical tensors M_1 and M_2 . Comparisons are also made with previous results using the version of AFFF with no angle and covalent harmonic interaction defined for sulfates [14]. When ettringite is considered, the most recent version of AFFF with covalent bonds and angles defined for

Table 4
Fitting parameters of a linear relation using the data in Fig. 13.

	Ettringite	Meta (RH = 1 %)	Meta (RH = 0.1 %)
C_{11} [GPa]	$-0.028 T + 44.669$ ($R^2 = 0.66$)	$-0.081 T + 53.060$ ($R^2 = 0.75$)	$-0.065 T + 53.567$ ($R^2 = 0.57$)
C_{33} [GPa]	$-0.012 T + 49.527$ ($R^2 = 0.38$)	$-0.052 T + 55.444$ ($R^2 = 0.32$)	$-0.002 T + 35.121$ ($R^2 = 0.00$)
C_{12} [GPa]	$0.008 T + 18.144$ ($R^2 = 0.25$)	$-0.072 T + 37.863$ ($R^2 = 0.67$)	$0.037 T + 6.794$ ($R^2 = 0.17$)
C_{13} [GPa]	$0.003 T + 17.992$ ($R^2 = 0.01$)	$-0.027 T + 23.571$ ($R^2 = 0.44$)	$0.026 T + 10.933$ ($R^2 = 0.28$)
C_{44} [GPa]	$-0.029 T + 18.742$ ($R^2 = 0.59$)	$-0.026 T + 16.104$ ($R^2 = 0.20$)	$-0.073 T + 30.487$ ($R^2 = 0.48$)
C_{66} [GPa]	$-0.010 T + 10.581$ ($R^2 = 0.27$)	$-0.035 T + 17.457$ ($R^2 = 0.34$)	$-0.019 T + 12.892$ ($R^2 = 0.06$)

sulfates [17] yields a Riemann metric closer to the experimental value and with a similar value obtained from DFT simulations [12] ($d_R/d_0=0.0027$ in this case as computed in ref. [17]). This result shows that introducing 2- and 3-body harmonic interactions in sulfates improves the description of the elasticity of ettringite.

The universal anisotropy index A^u defined as [47]:

$$A^u = 5 \frac{G_V}{G_R} + \frac{K_V}{K_R} - 6 \quad (21)$$

quantify the extent of anisotropy in crystals. For a locally isotropic crystal $A^u = 0$. The values of A^u for ettringite and metaettringite are shown in Table 3. According to this measure, metaettringite is less anisotropic than ettringite, which is expected due to the increase in

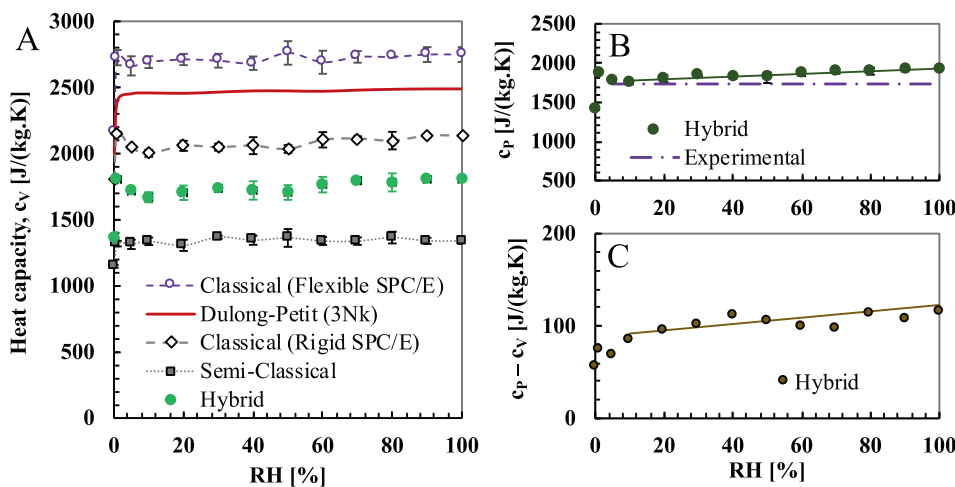


Fig. 9. (A) Comparison of the specific heat capacity c_V at constant volume of ettringite (and metaettringite) obtained using full classical methods (when rigid or flexible SPC/E water models are adopted), semi-classical and hybrid approaches. Dulong-Petit estimate ($3Nk$) is shown for comparison. (B) Heat capacity c_p at constant pressure, according to the hybrid approach, of ettringite (and metaettringite) as function of the RH compared with experimental data from refs [21,48]. (C) $c_p - c_V$ of ettringite (and metaettringite) function of the RH computed from the full rigidity tensor and tensor of thermal expansion (only the hybrid approach is shown). All results refers to ambient temperature (298 K).

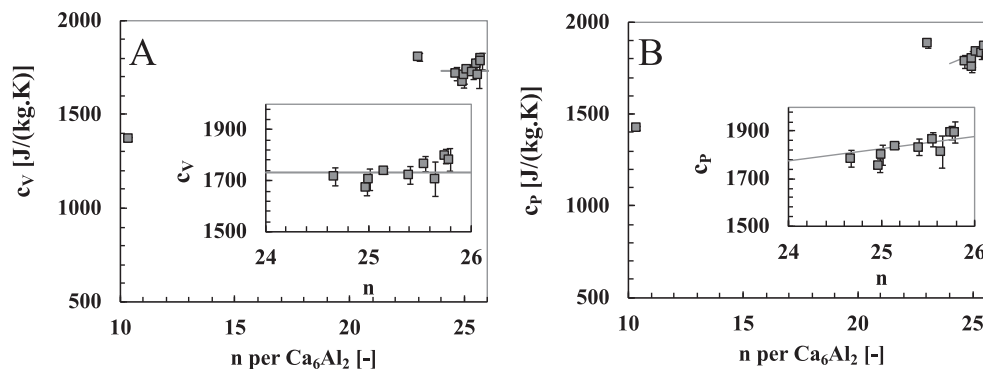


Fig. 10. Specific heat capacity at constant (A) volume and (B) pressure of ettringite (and metaettringite) at ambient temperature (298 K) as a function of the water content. The lines shows the average c_V and fitted c_p in the ettringite domain (RH >10 %). The inset zooms in the ettringite domain.

disorder observed in the conversion of ettringite into metaettringite [21].

3.1.4. Heat capacity

Fig. 9(A) shows the comparison of the heat capacity C_V at constant volume of ettringite (and metaettringite) obtained using full classical, full semi-classical, and the hybrid approaches. For the full classical approaches, cases with rigid and flexible SPC/E water models are shown; and both cases lead to overestimating the heat capacity of ettringite. The case with flexible SPC/E exceeds the Dulong-Petit estimate for the heat capacity, as expected due to the additional degree of freedom associated with intra-molecular vibrations [24]. The comparison with experiments shows that the full classical approaches cannot capture ettringite heat capacity correctly. Incorporating some quantum effects is needed, as is the case of the semi-classical method. The full semi-classical approach underestimates the heat capacity. The semi-classical applied to water underestimates the heat capacity of water [24], which justifies the hybrid approach. The hybrid approach lead to results in agreement with the experimental data [21,48]. Details on the velocity auto-correlation functions and vibrational density of states obtained for ettringite and metaettringite are given in Appendix B.

As for the other thermoelastic properties, the heat capacity c_V at constant volume remains stable for RH from 10 to 100 % (i.e., in the ettringite domain) with a decrease in the metaettringite domain. On the other hand, the heat capacity c_p at constant pressure shows a slight increase also in the ettringite domain: the line fitting the points in ettringite domain shown in Fig. 9(B) gives $c_p = 1.48RH + 1667$ (in J/(kg.K)). In terms of water content (Fig. 10) $c_p = 1.70n + 1758$ in

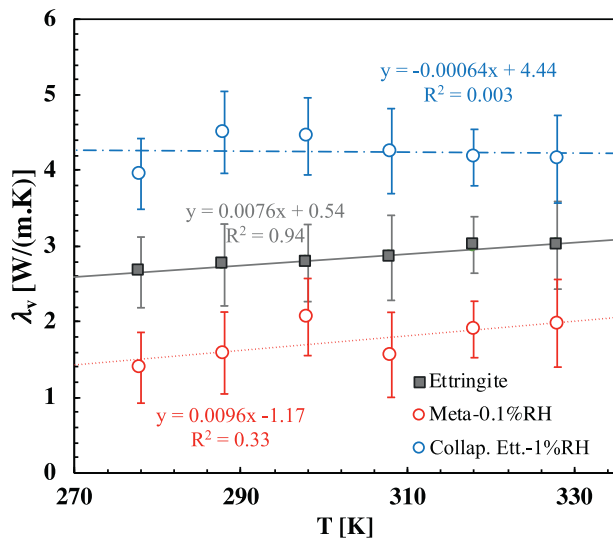


Fig. 11. Temperature-dependence of the volumetric thermal conductivity of ettringite and metaettringite. Twenty MD trajectories are considered to compute the standard deviations. Dashed lines are the least-squares linear fits. The coefficients of determination R^2 are also provided for each fitting.

ettringite domain. The hybrid simulations gives therefore $c_p=1454\text{--}1920$ J/(kg.K) for RH ranging from 10 to 100 %; 1879 J/(kg.K) for collapsing ettringite, and 1422 J/(kg.K) for metaettringite. Table 1 also gathers the data on the heat capacity from simulations. These values are to be compared with the experimental data available on ettringite: $c_p=1300$ J/(kg.K) [3,49], $c_p = 1717\text{--}1732$ J/(kg.K) [21], $c_p = 1732$ J/(kg.K) [48]. Experimental data on metaettringite gives $c_p=1489\text{--}1547$ J/(kg.K) [21].

3.2. Temperature dependence of thermoelastic properties

The temperature-dependence of the volumetric thermal conductivity (Fig. 11), volumetric coefficient of thermal expansion (Fig. 12), elastic constants (Fig. 13), and heat capacity (Fig. 14) of ettringite and metaettringite is studied in the temperature ranging from 278 to 328 K. Undrained conditions (i.e., water is not allowed to leave or ingress in the ettringite structure due to temperature changes) are adopted. Least-squares linear fitting is provided for all the cases considered.

There is a lack of experimental data on ettringite regarding the evolution of the thermoelastic properties with the temperature. The available data concerns the temperature dependence of c_p reported by

Ederova and Satava [48]: $c_p = 0.63T + 1545$ for c_p in J/(kg.K) and T in Kelvin. The variation of c_p with T observed in experiments is smaller than the one obtained from the simulations. The differences observed can arise from the semi-classical simulations per se, which neglects quantum effects in water confined in ettringite. Compared to the full classical approach, quantum corrections would decrease the heat capacity of water leading to a reduction therefore of the total heat capacity of ettringite. In this way, the hybrid approach as presented here functions as an upper bound for ettringite heat capacity, and the full semi-classical as a lower bound. A possible improvement to this work would be separating the contributions of apical (possibly more constrained) and zeolitic water (less constrained): treating apical water with the semi-classical approach would reduce the total heat capacity computed for ettringite, but keeping it higher than the semi-classical approach since zeolitic water would still be treated in the classical approach. Water exchange with neighboring porosity may also contribute to changes in the apparent heat capacity in experiments, but this contribution would lead to an increase in the apparent heat capacity [24]. Also, since Ederova and Satava [48] data was obtained in 1979, it should not be excluded the possibility that new measurements with more precise equipment may yield new temperature evolution that might be closer to what is observed in simulations.

Considering the standard deviations obtained from simulations, the volumetric thermal conductivities (Fig. 11) of ettringite, collapsing ettringite and metaettringite domains are statistically distinct. It is unclear why the thermal conductivity of collapsing ettringite is larger than that of ettringite and metaettringite. A possible reason would be that the columnar framework in collapsing ettringite remains mostly intact, contributing to phonon propagation (better than in the disordered metaettringite) but with a less significant disturbing effect on the water molecules (as in the ettringite domain).

The coefficients of thermal expansion (Fig. 12) obtained from simulations in ettringite, collapsing ettringite, and metaettringite domains are statistically indistinguishable in the range of temperatures tested when one considers the standard deviations obtained from simulations.

Regarding the elastic constants (Fig. 13), considering the standard deviations obtained from simulations, the values of C44, C66 and C13 are statistically indistinguishable in the range of temperatures tested. The axial elastic response along c-direction C33 (i.e., parallel to the columns) is larger in the ettringite domain, decreasing with the column collapsing, reaching the lower value for metaettringite (where no ordered columns are clearly identifiable). Along a-direction (and b-direction), C11 is statistically indistinguishable for ettringite and metaettringite but with a decrease in the collapsing ettringite. This decrease may be due to the water depletion at an almost constant volume which leaves voids in the crystal structure: in other words, apical

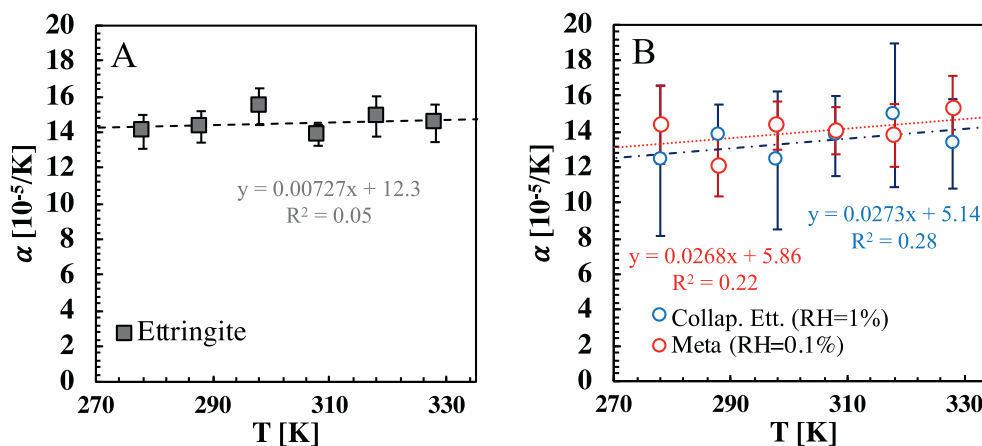


Fig. 12. Temperature-dependence of the volumetric coefficient of thermal expansion α_v , of (A) ettringite and (B) metaettringite. Least-squares linear fits and the corresponding coefficients of determination (R^2) are shown for each case.

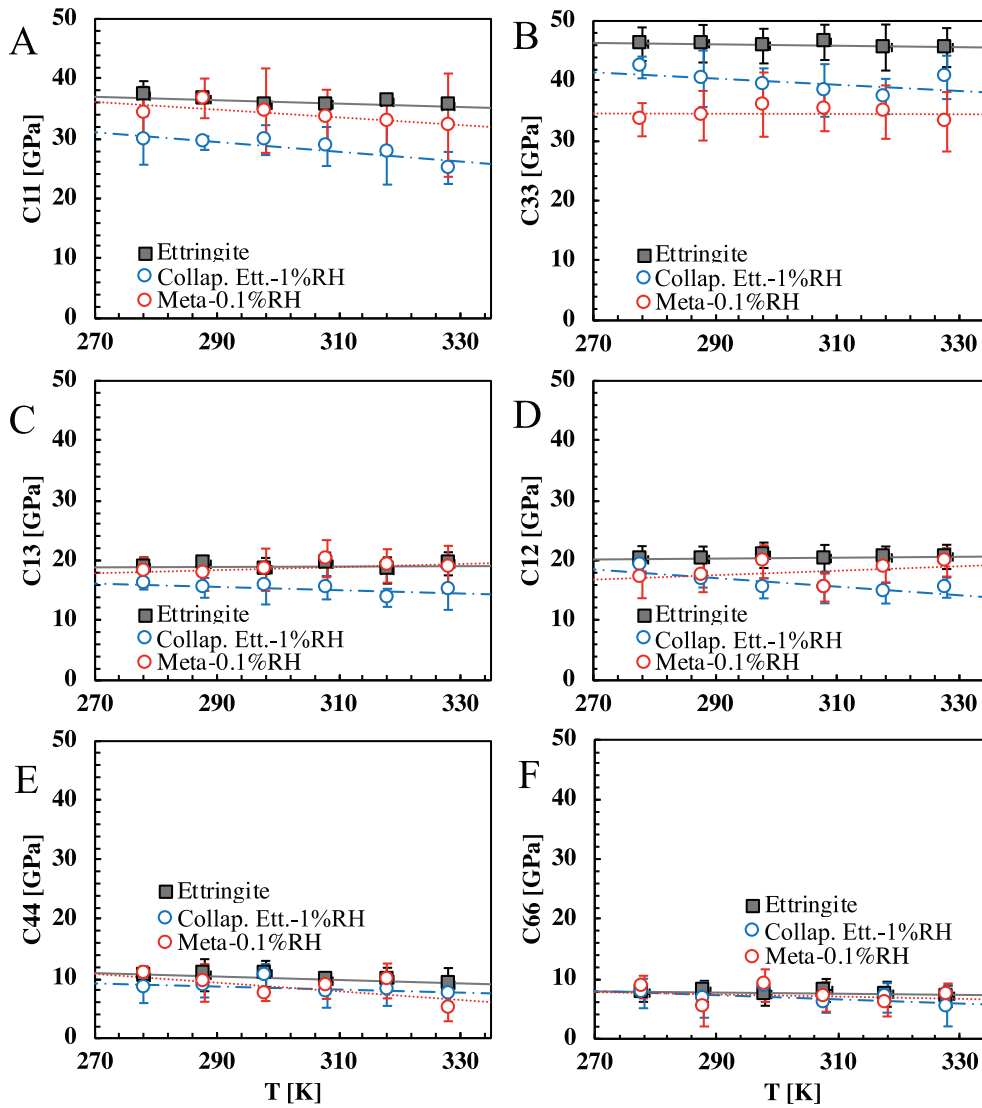


Fig. 13. Temperature-dependence of the elastic constants of ettringite and metaettringite. Least-squares linear fits and the corresponding coefficients of determination (R^2) are shown for each case in Table 4.

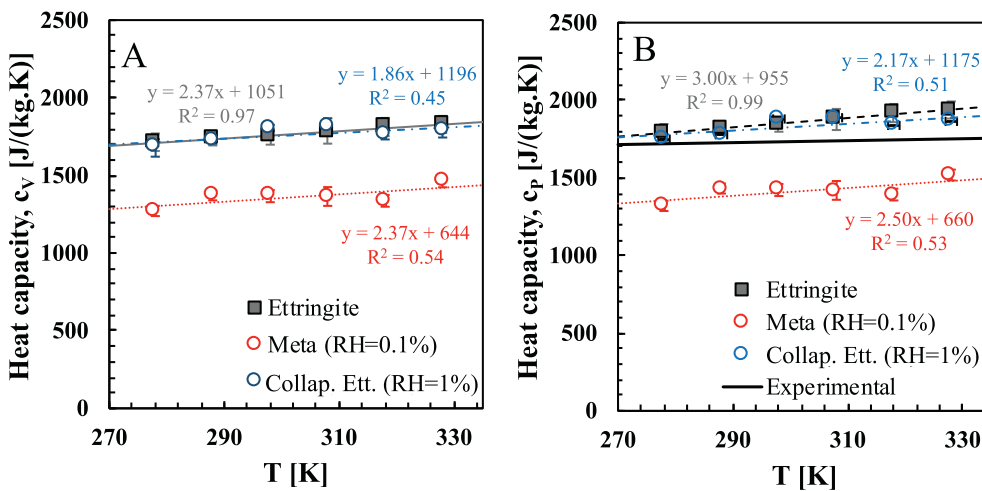


Fig. 14. Temperature-dependence of the heat capacity (A) c_v and (B) c_p of ettringite and metaettringite. Least-squares linear fits and the corresponding coefficients of determination (R^2) are shown for each case.

and zeolitic water would contribute to the larger rigidity of ettringite. The larger rigidity of metaettringite compared to collapsing ettringite might be due to the higher density of the former. The same arguments apply to the components coupling a and b, and a and c directions (i.e., C12 and C13).

4. Conclusion

Molecular simulations were deployed to quantify the thermoelastic properties of ettringite, collapsing ettringite and metaettringite. For the first time, the RH-dependence of these properties is quantified accounting for the anisotropies in the thermal conductivity, elastic constants, and coefficient of thermal expansion tensors. As expected, properties change with the RH is more pronounced at the low RH range since more significant structural changes occur in that range. For RH ranging from 10 to 100 % RH, the thermoelastic properties considered fluctuate around an average value, with fluctuations in the order of the standard deviation of the simulation results. In this RH range, the ettringite's thermoelastic properties can be considered a constant at ambient temperature. This observation allows defining a domain for ettringite (for RH ranging from 10 to 100 %) in which the thermoelastic properties can be approximated as a constant.

The heat capacity and thermal expansion of ettringite obtained from simulation are close to the available experimental data [3,41,48]. A hybrid approach combining a semi-classical method, in which some quantum effects are accounted for, and a full classical method for confined water is required to capture the experimental heat capacity of ettringite. This is in agreement with previous studies showing that full classical approaches often overestimate the heat capacity of crystals [7,34–36]. Still, that anharmonicity in water is better accounted for in a full classical approach with rigid models [24,50]. The ettringite's thermal conductivity and expansion are anisotropic, respecting the hexagonal crystal symmetry. Collapsing ettringite and metaettringite preserves the hexagonal symmetry.

The temperature dependence of the thermoelastic properties is quantified under undrained conditions. In most cases, the evolution of properties with the temperature can be fairly approximated as a linear evolution.

The values provided in this work for the thermoelastic properties of ettringite and metaettringite are fundamental data for multiscale modeling and predicting the thermal behavior of ettringite-rich materials. As a perspective, the effects of the temperature under drained (i.e., when water is allowed to leave or ingress in the ettringite structures due to temperature changes) conditions on the thermal properties of ettringite can also be quantified using a similar strategy and GCMC simulations.

CRedit authorship contribution statement

Tulio Honorio: Conceptualization, Methodology, Investigation, Formal analysis, Writing– original draft, Writing– review & editing, Validation.

Declaration of competing interest

The author declare no conflict of interest.

Appendix A. Thermal conductivity and heat capacity of bulk SPC/E water

Rigid SPC/E model is recognized to better capture the heat capacity of bulk water than flexible SPC/E [24,50,51]. The values reported for (bulk) rigid SPC/E water are

- $c_p = 4513.39$ J/(kg·K) and $c_v = 4123.49$ J/(kg·K) [50]
- $c_p = 4516$ J/(kg·K) and $c_v = 4127$ J/(kg·K) [51].

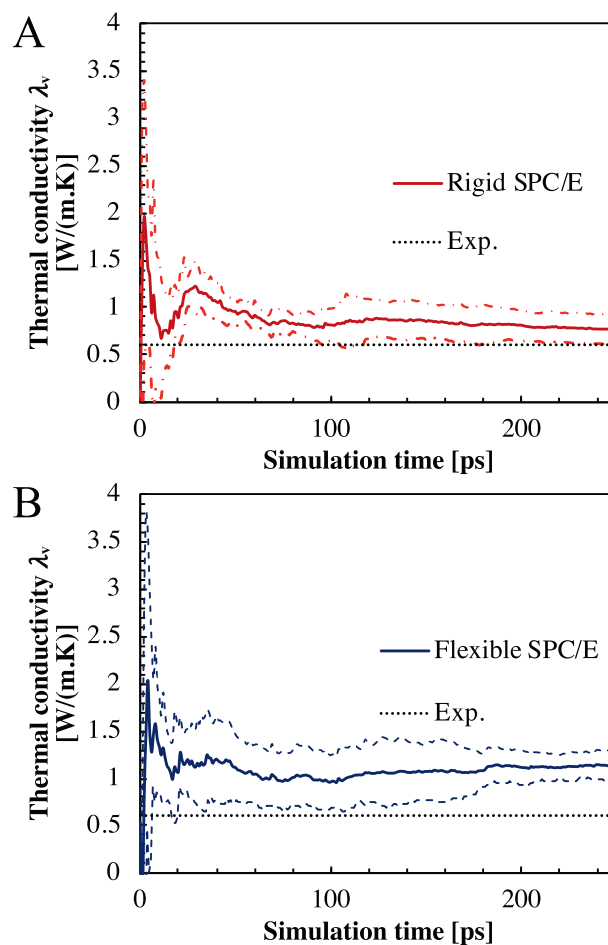


Fig. 15. Thermal conductivity of bulk SPC/E water: (A) rigid and (B) flexible models compared with the experimental value (dotted black line). Dashed lines depict the standard deviations of each simulation.

- $c_v = 4400 \pm 108$ J/(kg·K) [24].

The experimental values for c_p and c_v of bulk water are 4181.3 J/(kg·K) and 4137.6 J/(kg·K), respectively [52]. Flexible SPC/E (with ClayFF parameters for angle and bonds [23]) gives $c_v = 6252 \pm 592$ J/(kg·K).

In semi-classical estimates of the heat capacity, particles are treated as harmonic oscillators. Therefore, all the effects of anharmonicity in the interaction are not accounted for. This approximation is valid for crystalline water or water in the solid-state but leads to underestimations of liquid bulk water heat capacity [24]. Research on clays shows that the heat capacity of the clays solid layers (in the case montmorillonite with OH groups present) is best captured using the semi-classical approach instead of a full classical approach. In the same way, as shown in the current work, a semi-classical approach is expected to lead to better estimations of the heat capacity of ettringite columns.

Regarding the thermal conductivity of bulk SPC/E water, results using rigid and flexible SPC/E models are shown in Fig. 15. Both models overestimate the thermal conductivity of water. The rigid model yields result closer to the experimental value.

Appendix B. Velocity auto-correlation functions and vibrational density of states in ettringite and metaettringite

Fig. 16(A) and (B) shows the normalized total velocity auto-correlation $\langle \mathbf{v}_j(t) \cdot \mathbf{v}_j(0) \rangle / \langle v_j(0)^2 \rangle$, and normalized mass-weighted velocity auto-correlation $\langle m_j \mathbf{v}_j(t) \cdot \mathbf{v}_j(0) \rangle / \langle m_j v_j(0)^2 \rangle$ functions required to

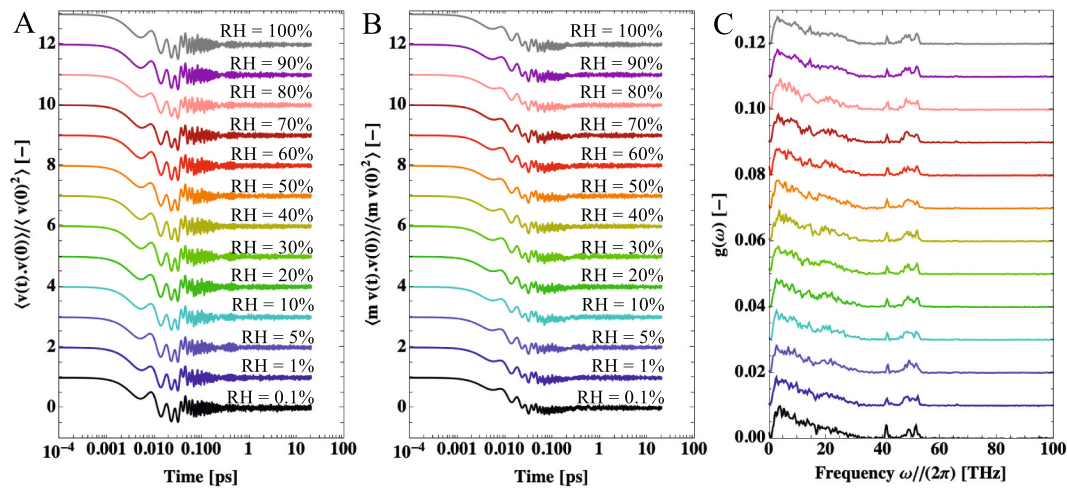


Fig. 16. (A) normalized total velocity auto-correlation $\langle v(t) \cdot v(0) \rangle / \langle v(0)^2 \rangle$, (B) normalized mass-weighted velocity auto-correlation $\langle m v(t) \cdot v(0) \rangle / \langle m v(0)^2 \rangle$, and (C) vibrational density of states $g(\omega)$ per RH at ambient temperature (298 K).

compute the vibrational density of states $g(\omega)$ in the semi-classical approach.

To identify the full range in which the VDOS does not vanish, frequencies exceeding 1000 THz were considered for selected cases. It was observed that the $g(\omega)$ vanished for $\omega / (1\pi)$ exceeding 70 THz. Therefore, the integration of $g(\omega)$ can be performed up to this frequency only in Eq. (9).

References

- H. F. W. Taylor C. Famy K. L. Scrivener, Delayed Ettringite Formation 31 (5) 683–693. doi:10.1016/S0008-8846(01)00466-5. URL <http://www.sciencedirect.com/science/article/pii/S0008884601004665>.
- B. Chen F. Kuznik M. Horgnies K. Johannes V. Morin E. Gengembre, Physicochemical properties of ettringite/meta-ettringite for thermal energy storage: Review 193 320–334. doi:10.1016/j.solmat.2018.12.013. URL <http://www.sciencedirect.com/science/article/pii/S0927024818305828>.
- L.J. Struble, P.W. Brown, An evaluation of ettringite and related compounds for use in solar energy storage, URL <https://nvlpubs.nist.gov/nistpubs/Legacy/IR/nbsir84-2942.pdf>, <https://doi.org/10.6028/NBS.IR.84-2942>.
- K. Ndiaye S. Ginestet M. Cyr, Modelling and Experimental Study of Low Temperature Energy Storage Reactor Using Cementitious Material 110 601–615. doi:10.1016/j.applthermaleng.2016.08.157. URL <http://www.sciencedirect.com/science/article/pii/S1359431116315162>.
- K. Ndiaye M. Cyr S. Ginestet, Durability and Stability of an Ettringite-based Material for Thermal Energy Storage at Low Temperature 99 106–115. doi:10.1016/j.cemconres.2017.05.001. URL <http://www.sciencedirect.com/science/article/pii/S0008884616306202>.
- J. W. Bullard E. J. Garboczi P. E. Stutzman P. Feng A. S. Brand L. Perry J. Hagedorn W. Griffin J. E. Terrill, Measurement and Modeling Needs for Microstructure and Reactivity of Next-generation Concrete Binders doi:10.1016/j.cemconcomp.2017.06.012. URL <http://www.sciencedirect.com/science/article/pii/S0958946517300823>.
- M.J.A. Qomi, F.-J. Ulm, R.J.-M. Pellenq, Physical origins of thermal properties of cement paste, Phys. Rev. Appl. 3 (6) (2015), 064010, <https://doi.org/10.1103/PhysRevApplied.3.064010>. <http://link.aps.org/doi/10.1103/PhysRevApplied.3.064010>.
- S.-N. Hong, C.-J. Yu, U.-S. Hwang, C.-H. Kim, B.-H. Ri, Effect of porosity and temperature on thermal conductivity of jennite: a molecular dynamics study, Mater. Chem. Phys. 250 (2020), 123146, <https://doi.org/10.1016/j.matchemphys.2020.123146>. <https://www.sciencedirect.com/science/article/pii/S0254058420305186>.
- P.K. Sarkar, N. Mitra, Thermal conductivity of cement paste: influence of macro-porosity, Cem. Concr. Res. 143 (2021), 106385, <https://doi.org/10.1016/j.cemconres.2021.106385>. <https://www.sciencedirect.com/science/article/pii/S000888462100034X>.
- H. Manzano A. Ayuela A. Telesca P. J. M. Monteiro J. S. Dolado, Ettringite Strengthening at High Pressures Induced by the Densification of the Hydrogen Bond Network 116 (30) 16138–16143. doi:10.1021/jp301822e. URL <http://pubs.acs.org/doi/10.1021/jp301822e>.
- E. Scholtzová D. Tunega S. Speziale, Mechanical Properties of Ettringite and Thaumassite—DFT and Experimental Study 77 9–15. doi:10.1016/j.cemconres.2015.06.008. URL <http://www.sciencedirect.com/science/article/pii/S0008884615001775>.
- E. Scholtzová L. Kucková J. Kožšek D. Tunega, Structural and Spectroscopic Characterization of Ettringite Mineral—Combined DFT and Experimental Study 1100 215–224. doi:10.1016/j.molstruc.2015.06.075. URL <https://linkinghub.elsevier.com/retrieve/pii/S0022286015301022>.
- L. Liu A. Jaramillo-Botero W. A. Goddard H. Sun, Development of a ReaxFF Reactive Force Field for Ettringite and Study of its Mechanical Failure Modes From Reactive Dynamics Simulations 116 (15) 3918–3925. doi:10.1021/jp210135j. URL <http://pubs.acs.org/doi/10.1021/jp210135j>.
- T. Honorio P. Guerra A. Bourdot, Molecular Simulation of the Structure and Elastic Properties of Ettringite and Monosulfoaluminate 135 106126. doi:10.1016/j.cemconres.2020.106126. URL <http://www.sciencedirect.com/science/article/pii/S0008884619306714>.
- W. Sun D. Wang L. Wang, Molecular Dynamic Simulation of Failure of Ettringite 419 012011. doi:10.1088/1742-6596/419/1/012011. URL <http://stacks.iop.org/1742-6596/419/i=1/a=012011?key=crossref.446991660526c03931dbb498844696e3>.
- A. G. Kalinichev R. J. Kirkpatrick, Molecular Dynamics Modeling of Chloride Binding to the Surfaces of Calcium Hydroxide, Hydrated Calcium Aluminate, and Calcium Silicate Phases 14 (8) 3539–3549. doi:10.1021/cm0107070. URL <https://doi.org/10.1021/cm0107070>.
- T. Honorio, M. Maaroufi, S. Al Dandachli, A. Bourdot, Ettringite hysteresis under sorption from molecular simulations, URL, Cem. Concr. Res. 150 (2021), 106587, <https://doi.org/10.1016/j.cemconres.2021.106587>, <https://linkinghub.elsevier.com/retrieve/pii/S0008884621002362>.
- Q. Zhou E. Lachowski F. Glasser, Metaettringite, A Decomposition Product of Ettringite 34 (4) 703–710. doi:10.1016/j.cemconres.2003.10.027.
- Y. Du, Y. Ge, Multiphase model for predicting the thermal conductivity of cement paste and its applications, URL, Materials 14 (16) (2021) 4525, <https://doi.org/10.3390/ma14164525>, <https://www.mdpi.com/1996-1944/14/16/4525>.
- N. N. Skoblinkaya K. G. Krasilnikov, Changes in Crystal Structure of Ettringite on Dehydration. 1 5 (4) 381–393. doi:10.1016/0008-8846(75)90093-9. URL <http://www.sciencedirect.com/science/article/pii/0008884675900939>.
- L. G. Baquerizo T. Matschei K. L. Scrivener, Impact of Water Activity on the Stability of Ettringite 79 31–44. doi:10.1016/j.cemconres.2015.07.008. URL <http://www.sciencedirect.com/science/article/pii/S0008884615001970>.
- A. E. Moore H. F. W. Taylor, Crystal Structure of Ettringite 26 (4) 386–393. doi:10.1107/S0567740870002443. URL <https://scripts.iucr.org/cgi-bin/paper?a07390>.
- R. T. Cygan J. A. Greathouse A. G. Kalinichev, Advances in Clayff molecular simulation of layered and nanoporous materials and their aqueous interfaces, J. Phys. Chem. C Publisher: American Chemical Society. doi:10.1021/acs.jpcc.1c04600. URL <https://doi.org/10.1021/acs.jpcc.1c04600>.
- T. Honorio, L. Brochard, Drained and undrained heat capacity of swelling clays, Phys. Chem. Chem. Phys. (2022), <https://doi.org/10.1039/D2CP01419J> doi: 10.1039/D2CP01419J.
- S. Plimpton, Fast Parallel Algorithms for Short-range Molecular Dynamics 117 (1) 1–19. doi:10.1006/jcph.1995.1039. URL <http://www.sciencedirect.com/science/article/pii/S002199918571039X>.
- T. Ikeshoji, B. Hafskjold, Non-equilibrium molecular dynamics calculation of heat conduction in liquid and through liquid-gas interface, publisher: Taylor & Francis eprint: Mol. Phys. 81 (2) (1994) 251–261, <https://doi.org/10.1080/00268979400100171>. URL <https://doi.org/10.1080/00268979400100171>, <https://doi.org/10.1080/00268979400100171>, <https://doi.org/10.1080/00268979400100171>.
- F. Müller-Plathe, A simple nonequilibrium molecular dynamics method for calculating the thermal conductivity, URL, J. Chem. Phys. 106 (14) (1997) 6082–6085, <https://doi.org/10.1063/1.473271>, <https://aip.scitation.org/doi/abs/10.1063/1.473271>.
- J. P. Boon S. Yip, Molecular Hydrodynamics, Courier Corporation, google-Books-ID: LfCDDwAAQBAJ.

- [29] K. Termentzidis S. Merabia P. Chantrenne P. Keblinski , Cross-plane thermal conductivity of superlattices with rough interfaces using equilibrium and non-equilibrium molecular dynamics, *Int. J. Heat Mass Transf.* 54 (9-10). doi:10.1016/j.ijheatmasstransfer.2011.01.001.
- [30] T. Cagin N. Karasawa S. Dasgupta W. A. Goddard , Thermodynamic and elastic properties of polyethylene at elevated temperatures, *MRS Online Proceedings Library Archive* 278.
- [31] J.R. Ray, Molecular dynamics equations of motion for systems varying in shape and size, *J. Chem. Phys.* 79 (10) (1983) 5128–5130, <https://doi.org/10.1063/1.445636>.
- [32] T. Honorio T. Lemaire D. D. Tommaso S. Naili , Molecular Modelling of the Heat Capacity and Anisotropic Thermal Expansion of Nanoporous Hydroxyapatite 100251 doi:10.1016/j.jmmla.2019.100251. URL <http://www.sciencedirect.com/science/article/pii/S258915291930047X>.
- [33] M.P. Allen, D.J. Tildesley, *Computer Simulation of Liquids*, Oxford University Press, New York, 1989.
- [34] B. Winkler M. T. Dove , Thermodynamic Properties of MgSiO₃ Perovskite Derived From Large Scale Molecular Dynamics Simulations 18 (7) 407–415. doi:10.1007/BF00200963. URL <https://doi.org/10.1007/BF00200963>.
- [35] A.R. Oganov, J.P. Brodholt, G.David Price, Comparative study of quasiharmonic lattice dynamics, molecular dynamics and Debye model applied to MgSiO₃ perovskite, *Phys. Earth Planet. Inter.* 122 (3) (2000) 277–288, [https://doi.org/10.1016/S0031-9201\(00\)00197-7](https://doi.org/10.1016/S0031-9201(00)00197-7), google-Books-ID: bNDMBQAAQBAJ, <https://www.sciencedirect.com/science/article/pii/S0031920100001977>.
- [36] J. Claverie, S. Kamali-Bernard, J.M.M. Cordeiro, F. Bernard, Assessment of mechanical, thermal properties and crystal shapes of monoclinic tricalcium silicate from atomistic simulations, *Cem. Concr. Res.* 140 (2021), 106269, <https://doi.org/10.1016/j.cemconres.2020.106269>. <https://www.sciencedirect.com/science/article/pii/S0008884620315490>.
- [37] J.M. Dickey, A. Paskin, Computer simulation of the lattice dynamics of solids, *Phys. Rev.* 188 (3) (1969) 1407–1418, <https://doi.org/10.1103/PhysRev.188.1407>. <https://link.aps.org/doi/10.1103/PhysRev.188.1407>.
- [38] P.H. Berens, D.H.J. Mackay, G.M. White, K.R. Wilson, Thermodynamics and quantum corrections from molecular dynamics for liquid water, URL, *J. Chem. Phys.* 79 (5) (1998) 2375, <https://doi.org/10.1063/1.446044>, <https://aip.scitation.org/doi/abs/10.1063/1.446044>.
- [39] D.C. Wallace, *Thermodynamics of Crystals*, Courier Corporation, 1998 google-Books-ID: qLzOmwSgMlSc.
- [40] J. Thomas, R.R. Frost, R.D. Harvey, Thermal conductivity of carbonate rocks, *Eng. Geol.* 7 (1) (1973) 3–12, [https://doi.org/10.1016/0013-7952\(73\)90003-3](https://doi.org/10.1016/0013-7952(73)90003-3). <https://www.sciencedirect.com/science/article/pii/0013795273900033>.
- [41] C. Hall, P. Barnes, A.D. Billimore, A.C. Jupe, X. Turrillas, Thermal decomposition of ettringite Ca₆[Al(OH)₆]₂(SO₄)₃A·26H₂O, URL, *J. Chem. Soc. Faraday Trans.* 92 (12) (1996) 2125–2129, <https://doi.org/10.1039/FT9969202125>, <https://pubs.rsc.org/en/content/articlelanding/1996/ft9969202125>.
- [42] R. Hill, The elastic behaviour of a crystalline aggregate, *Proc. Phys. Soc. London, Sect. A* 65 (5) (1952) 349, <https://doi.org/10.1088/0370-1298/65/5/307>. <http://stacks.iop.org/0370-1298/65/i=5/a=307>.
- [43] I.R. Shein, A.L. Ivanovskii, Elastic properties of mono- and polycrystalline hexagonal AlB₂-like diborides of s, p and d metals from first-principles calculations, *J. Phys. Condens. Matter* 20 (41) (2008), 415218, <https://doi.org/10.1088/0953-8984/20/41/415218>. <https://iopscience.iop.org/article/10.1088/0953-8984/20/41/415218>.
- [44] S. Speziale, F. Jiang, Z. Mao, P.J.M. Monteiro, H.-R. Wenk, T.S. Duffy, F. R. Schilling, Single-crystal elastic constants of natural ettringite, *Cem. Concr. Res.* 38 (7) (2008) 885–889, <https://doi.org/10.1016/j.cemconres.2008.02.004>. <http://www.sciencedirect.com/science/article/pii/S0008884608000471>.
- [45] M. Moakher, On the averaging of symmetric positive-definite tensors, *J. Elast.* 82 (3) (2006) 273–296, <https://doi.org/10.1007/s10659-005-9035-z>, doi: 10.1007/s10659-005-9035-z.
- [46] R. Shahsavari, R.J.-M. Pellenq, F.-J. Ulm, Empirical force fields for complex hydrated calcio-silicate layered materials, *Phys. Chem. Chem. Phys.* 13 (3) (2010) 1002–1011, <https://doi.org/10.1039/C0CP00516A>.
- [47] S.I. Ranganathan, M. Ostoja-Starzewski, Universal elastic anisotropy index, *Phys. Rev. Lett.* 101 (5) (2008), 055504, <https://doi.org/10.1103/PhysRevLett.101.055504>. <https://link.aps.org/doi/10.1103/PhysRevLett.101.055504>.
- [48] J. Ederova, V. Satava, Heat capacities of C₃AH₆, C₄AH₁₂ and C₆AS₃H₃₂, *Thermochim. Acta* 31 (1) (1979) 126–128, [https://doi.org/10.1016/0040-6031\(79\)80016-7](https://doi.org/10.1016/0040-6031(79)80016-7). <https://www.sciencedirect.com/science/article/pii/0040603179800167>.
- [49] L.J. Struble, P.W. Brown, Heats of dehydration and specific heats of compounds found in concrete and their potential for thermal energy storage, *Solar Energy Mater.* 14 (1) (1986) 1–12, [https://doi.org/10.1016/0165-1633\(86\)90008-0](https://doi.org/10.1016/0165-1633(86)90008-0). <https://linkinghub.elsevier.com/retrieve/pii/0165163386900080>.
- [50] Y. Mao, Y. Zhang, Thermal conductivity, shear viscosity and specific heat of rigid water models, *Chem. Phys. Lett.* 542 (2012) 37–41, <https://doi.org/10.1016/j.cplett.2012.05.044>. <http://www.sciencedirect.com/science/article/pii/S0009261412006367>.
- [51] I. Shvab, R.J. Sadus, Atomistic water models: aqueous thermodynamic properties from ambient to supercritical conditions, *Fluid Phase Equilib.* 407 (2016) 7–30, <https://doi.org/10.1016/j.fluid.2015.07.040>. <https://linkinghub.elsevier.com/retrieve/pii/S0378381215300558>.
- [52] W.M. Haynes, *CRC Handbook of Chemistry and Physics*, 95th Edition, CRC Press, 2014 google-Books-ID: bNDMBQAAQBAJ.